



# UniMamba: Unified Spatial-Channel Representation Learning with Group-Efficient Mamba for LiDAR-based 3D Object Detection

Xin Jin<sup>♣,2,3,♡</sup> Haisheng Su<sup>♣,1,3(✉)</sup> Kai Liu<sup>3</sup> Cong Ma<sup>3</sup> Wei Wu<sup>3,4</sup> Fei HUI<sup>2(✉)</sup> Junchi Yan<sup>1(✉)</sup>

<sup>1</sup>School of Computer Science, Shanghai Jiao Tong University

<sup>2</sup>Chang’an University, <sup>3</sup>SenseAuto Research, <sup>4</sup>Tsinghua University

{suhaiheng, yanjunchi}@sjtu.edu.cn, {jinxin, feihui}@chd.edu.cn

{liukai3.iag, macong, wuwei}@senseauto.com

Code & Models: [UniMamba](#)

## Abstract

Recent advances in LiDAR 3D detection have demonstrated the effectiveness of Transformer-based frameworks in capturing the global dependencies from point cloud spaces, which serialize the 3D voxels into the flattened 1D sequence for iterative self-attention. However, the spatial structure of 3D voxels will be inevitably destroyed during the serialization process. Besides, due to the considerable number of 3D voxels and quadratic complexity of Transformers, multiple sequences are grouped before feeding to Transformers, leading to a limited receptive field. Inspired by the impressive performance of State Space Models (SSM), in this paper, we propose a novel Unified Mamba (UniMamba), which seamlessly integrates the merits of 3D convolution and SSM in a concise multi-head manner, aiming to perform “local and global” spatial context aggregation efficiently and simultaneously. Specifically, a UniMamba block is designed which mainly consists of spatial locality modeling, complementary Z-order serialization and local-global sequential aggregator. The spatial locality modeling module integrates 3D submanifold convolution to capture the dynamic spatial position embedding before serialization. Then the efficient Z-order curve is adopted for serialization both horizontally and vertically. Furthermore, the local-global sequential aggregator adopts the channel grouping strategy to efficiently encode both “local and global” spatial inter-dependencies using multi-head SSM. Additionally, an encoder-decoder architecture with stacked UniMamba blocks is formed to facilitate multi-scale spatial learning hierarchically. Extensive experiments are conducted on three popular datasets: nuScenes, Waymo and Argoverse 2. Particularly, our UniMamba achieves 70.2 mAP on the nuScenes dataset.

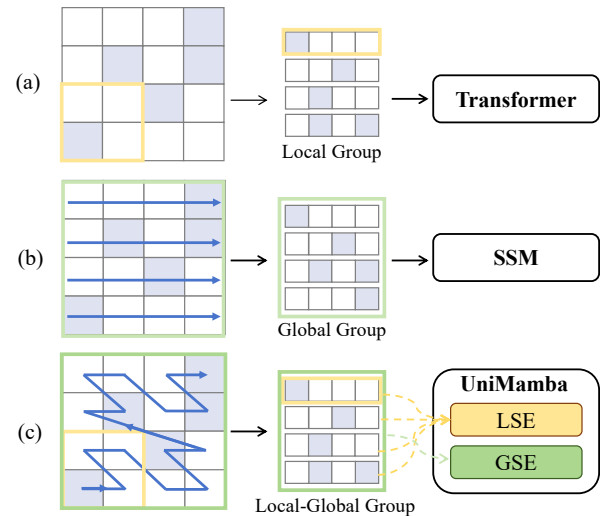


Figure 1. Comparison of different 3D backbones. (a) Transformer-based backbone using **local** window grouping. (b) SSM-based backbone using **global** sequence grouping. (c) Our proposed UniMamba backbone using channel-wise **local-global** grouping.

## 1. Introduction

LiDAR is widely used in Autonomous Driving perception tasks [35, 36] due to its ability to provide precise 3D location information. However, unlike structured image data, the sparsity and disorder of point cloud space pose significant challenges for accurate 3D object detection. Therefore, learning effective pattern representations from 3D point clouds is a key focus of current research.

Previous methods are generally classified into point-based and voxel-based approaches. Point-based methods [33, 46] directly apply operators such as PointNet [29, 30] to manipulate raw point clouds, which entails a time-consuming process of sampling and grouping, leading to low computational efficiency. In contrast, voxel-based methods [4, 44, 53] convert point clouds into regular grids, showcasing superior performance and becoming the domi-

♣ Equal Contribution. ✉ Corresponding Authors.  
♡ Intern at SenseAuto Research.

nant mainstream architecture.

Voxel-based methods can be further categorized into sparse convolution neural networks (SpCNN)-based and Transformer-based. SpCNN-based approaches [47, 49] are constrained by the inherently small receptive field of convolutions, which limits their ability to extract rich contextual information. Transformer-based methods [23, 27, 40] suffer from quadratic complexity, which tend to serialize 3D voxels into multiple 1D sequences and adopt self-attention mechanism respectively, leading to limited receptive field by group size and feature size (Fig. 1 (a)). However, both local structure details and global context are crucial [18, 19, 31] for 3D object detection from sparse and occluded point clouds. *Under this circumstance, a robust LiDAR 3D backbone with flexible receptive fields and great spatial modeling capacity as well as computational efficiency is worth exploring.*

Inspired by the remarkable success of the Mamba [10, 22, 24, 54] architecture in the areas of vision tasks, we investigate its applicability to LiDAR 3D detection. Its linear complexity enables the whole sequence processing without voxel grouping (Fig. 1 (b)), thus facilitating the global context modeling [50]. However, simple adaptation of Mamba to LiDAR 3D backbone may have some *drawbacks*: (1) loss of spatial voxel locality during serialization; (2) local redundancy brought by coherent global modeling, causing inferior efficiency; (3) lack of spatial diversity to handle complex local and global dependencies.

To this end, we propose **UniMamba**, a unified Mamba architecture to integrate 3D convolution and State Space Models (SSM) in a concise multi-head format, which can achieve a preferable balance between effectiveness and efficiency in spatial structure modeling for LiDAR 3D object detection. Specifically, our UniMamba consists of three main modules, namely spatial locality modeling, complementary Z-order serialization and local-global sequential aggregator. The Spatial Locality Modeling (SLM) module aims to capture the dynamic structure embedding with 3D submanifold sparse convolution before serialization. Then the complementary Z-order serialization is proposed to transform 3D voxels into 1D sequence, considering the spatial proximity preservation both horizontally and vertically. Subsequently, a Local-Global Sequential Aggregator (LGSA) is designed to perform “local-global” spatial aggregation in a group-efficient fashion (Fig. 1 (c)), which includes two sub-modules, *i.e.*, Local Sequential Encoder (LSE) and Global Sequential Encoder (GSE). Concretely, GSE processes all voxels in a single 1D sequence with multi-head bidirectional SSM, allowing global contextual modeling directly without multiple sub-sequence grouping. Contrary, LSE handles the grouped 1D sequences respectively to capture the local inter-dependencies. Besides, a channel grouping strategy is proposed to aggregate “local-

global” spatial context in parallel. Finally, through stacking our UniMamba blocks into an encoder-decoder architecture with several stages, our UniMamba exhibits great potential as LiDAR 3D backbone for multi-scale spatial relation modeling efficiently, achieving 70.2 mAP and 74.0 NDS on nuScenes test set particularly. In summary, the main contributions of our work can be summarized into three folds:

- We propose **UniMamba**, a novel unified 3D backbone for LiDAR 3D object detection, which integrates 3D convolution and bidirectional SSM to achieve effective spatial modeling in a group-efficient manner.
- We design a Local-Global Sequential Aggregator to simultaneously capture *local and global* voxel relations in a channel-grouping fashion, benefiting from the spatial locality modeling and complementary Z-order serialization in case of spatial proximity loss.
- Extensive experiments are conducted on three popular benchmarks, *i.e.*, nuScenes, Waymo and Argoverse 2, demonstrating the effectiveness of our UniMamba.

## 2. Related Work

Lidar-based 3D detectors are typically classified into point-based and voxel-based. Point-based methods [29, 30, 33, 46, 51] extract multi-scale local contextual features directly from downsampled raw points. However, the down-sampling and multi-scale grouping lead to a significant computational overhead, resulting in low inference speeds that limit their practical applications. Voxel-based detectors [44, 53] convert unordered point clouds into structured grids through voxelization and apply various backbones to extract 3D features, which have become mainstream frameworks for outdoor 3D detection tasks. According to the network architecture, 3D backbones can be classified into the following three categories.

### 2.1. 3D Object Detection with Sparse Convolution

VoxelNet [53] pioneered voxel-based detectors by directly utilizing regular convolution. However, due to the sparsity of point clouds, the direct application of 3D convolutions incurs significant computational costs and information redundancy. Therefore, existing methods [1, 3, 5, 6, 49] typically use sparse convolutional neural network (SpCNN) to extract features. Largekernel3D [4] migrate large convolutional kernels into the 3D detection domain, enhancing the inherent receptive field. HEDNet [48] learns long-range dependencies via a multi-scale encoder-decoder structure. These methods aim to improve the receptive field of SpCNN-based 3D backbones. However, the advantage of convolution lies in its powerful local information extraction capabilities and inductive bias. Therefore, in this paper, we combine SpCNN to compensate for the lack of locality in mamba when extracting long-range contextual information.

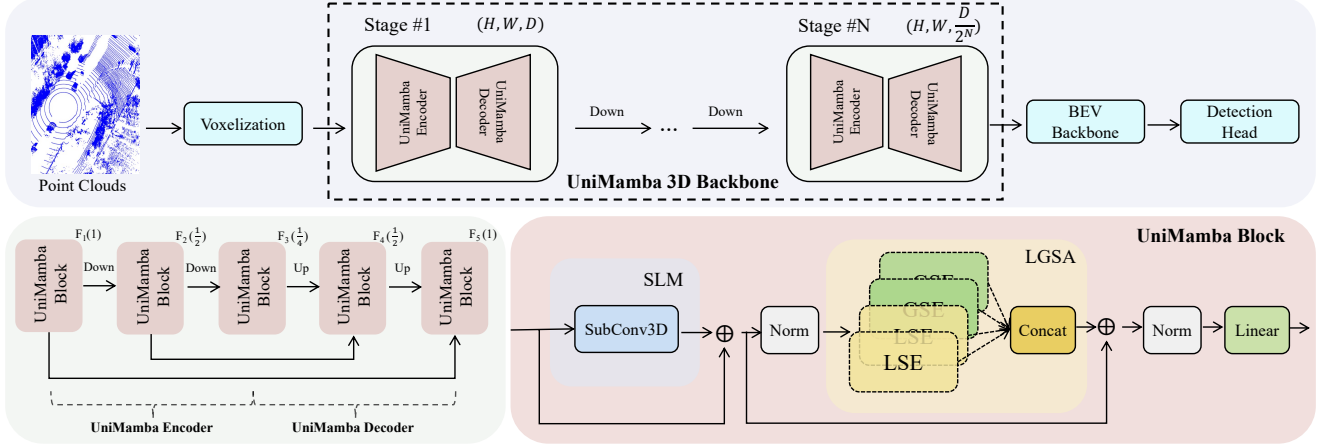


Figure 2. Illustration of our proposed UniMamba backbone, which consists of multiple stages, and each stage includes several UniMamba blocks to encode multi-scale features with an encoder-decoder architecture through down/up-sampling and stacking operations. The UniMamba Block is our core component, which efficiently enables simultaneous extraction and aggregation of *local and global* contextual information. In UniMamba, We first voxelize the point clouds, then adopt the proposed UniMamba 3D backbone to extract multi-scale rich spatial contextual features. Finally, these enhanced features are fed into a BEV backbone and a detection head for final 3D object detection.

## 2.2. 3D Object Detection with Transformer

Transformer [39] has been extensively researched in point cloud detection tasks. Due to computational efficiency constraints, it is impractical to directly compute the attention scores for all voxels. Existing methods [7, 23, 38, 40, 45, 52] typically employ a window-based attention mechanism, dividing the 3D space into multiple small windows, and then applying shift window or multi-scale fusion to achieve a global receptive field. However, small windows still limit the receptive field. In this paper, we utilize Mamba to replace Transformer, achieving larger window groupings, which addresses the issue of limited receptive fields while also providing better inference efficiency.

## 2.3. Vision Task with Mamba

Mamba [10] is a popular sequential modeling architecture with linear complexity. Due to its great computational efficiency, it has been regarded as a strong competitor to Transformer. Some research has begun to explore its potential in vision tasks [11, 15, 20–22]. As a sequence model, most existing studies have focused on exploring different scanning methods. Vim [54] introduced a bidirectional SSM to learn image features. GrootVL [43] adopted a tree topology to construct scanning sequences, enhancing long-range interactions. The most advanced lidar detectors utilized the Mamba architecture, while LION [24] developed a unified RNN framework using group-based strategy. VoxelMamba [50] introduced a group-free approach to directly model global information. In this paper, we investigate the feasibility of Mamba-style architecture for LiDAR 3D detection, and propose UniMamba, which can effectively capture local and global voxel interactions simultaneously.

## 3. Method

In this section, we introduce the specific architecture of UniMamba, which is a voxel-based 3D backbone integrating 3D convolution and bidirectional SSM to achieve effective spatial modeling in a group-efficient manner. First, we present the basic concepts of Mamba (Sec. 3.1), followed by an overview of UniMamba (Sec. 3.2). Then we describe the key components of the UniMamba block (Sec. 3.3) in detail. Finally, we provide a detailed analysis of the overall composition of our backbone (Sec. 3.4).

### 3.1. Preliminaries

Mamba is a powerful discrete variant of the State Space Model (SSM). The SSM is a continuous system that establishes a mapping between inputs  $x(t) \in \mathbb{R}^L$  and output  $y(t) \in \mathbb{R}^L$  through a hidden state vector  $h(t) \in \mathbb{R}^N$ . This system can be expressed as follows:

$$\begin{aligned} h'(t) &= \mathbf{A}h(t) + \mathbf{B}x(t), \\ y(t) &= \mathbf{C}h(t), \end{aligned} \quad (1)$$

where  $\mathbf{A} \in \mathbb{R}^{N \times N}$ ,  $\mathbf{B} \in \mathbb{R}^{N \times 1}$  and  $\mathbf{C} \in \mathbb{R}^{1 \times N}$  represent the learnable evolution parameters and the two projection parameters, respectively. To discretize it for fitting sequences and image data, the zero-order hold (ZOH) method is used to convert  $\mathbf{A}$  and  $\mathbf{B}$  into discrete parameters  $\bar{\mathbf{A}}$  and  $\bar{\mathbf{B}}$  with a time scale parameter  $\Delta$ . The conversion process is as follows:

$$\begin{aligned} \bar{\mathbf{A}} &= \exp(\Delta \mathbf{A}), \\ \bar{\mathbf{B}} &= (\Delta \mathbf{A})^{-1}(\exp(\Delta \mathbf{A}) - \mathbf{I}) \cdot \Delta \mathbf{B} \end{aligned} \quad (2)$$

Compared to previous SSMs, Mamba enhances contextual awareness by introducing a dynamic selective scanning mechanism (S6). Specifically, its parameters  $\mathbf{B} \in$

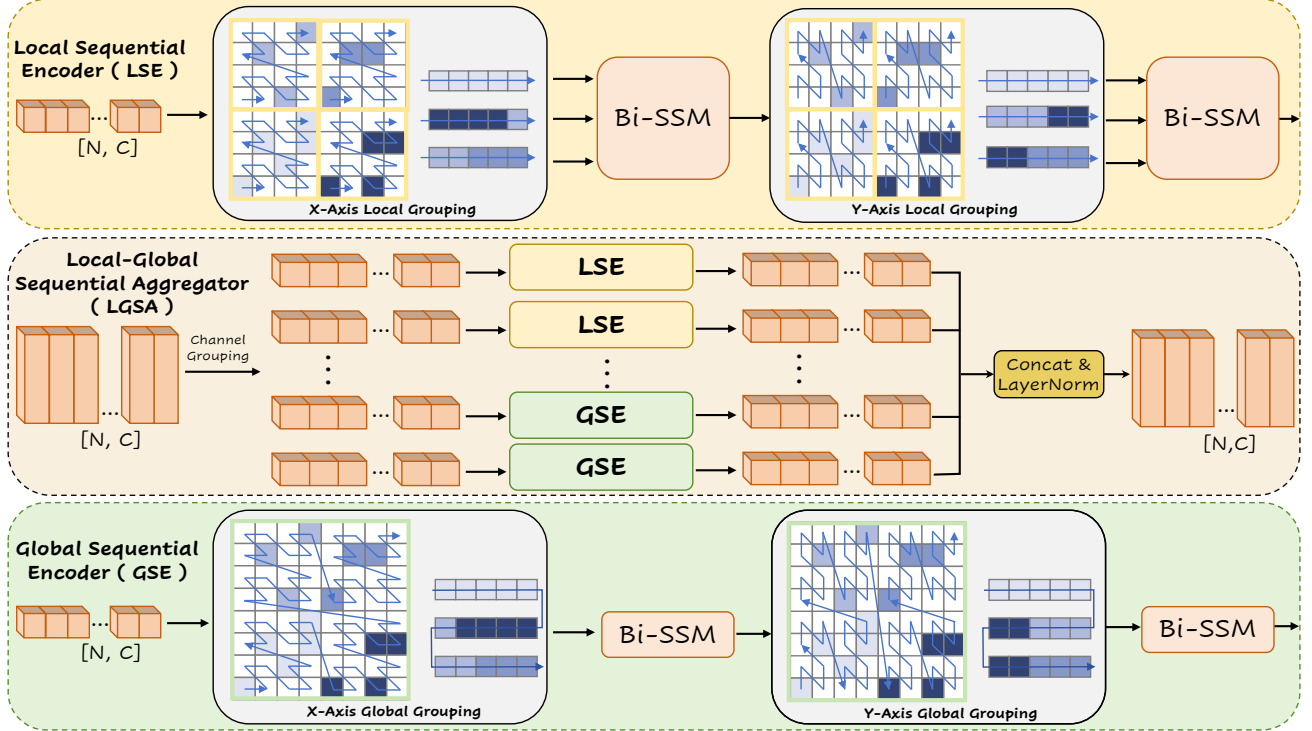


Figure 3. Illustration of Local-Global Sequential Aggregator. Local Sequential Encoder (LSE) adopts the bidirectional SSM to handle the multiple 1D groups respectively with the proposed complementary Z-order serialization both vertically and horizontally. Instead, Global Sequential Encoder (GSE) handles a single group without sequence partition to capture the global inter-dependencies. Then the Local-Global Sequential Aggregator (LGSA) combines these two encoders in a multi-head format through channel grouping, which can model both local structure details and global context information simultaneously.

$\mathbb{R}^{B \times L \times N}$ ,  $\mathbf{C} \in \mathbb{R}^{B \times L \times N}$  and  $\Delta \in \mathbb{R}^{B \times L \times D}$  are directly obtained from the input  $x \in \mathbb{R}^{B \times L \times D}$ . Thus, the discretized SSM can be expressed as:

$$\begin{aligned} h_t &= \bar{\mathbf{A}}h_{t-1} + \bar{\mathbf{B}}x_t, \\ y_t &= \mathbf{C}h_t. \end{aligned} \quad (3)$$

## 3.2. Overview

As shown in Fig. 2, UniMamba comprises four main components: the Voxel Feature Encoder, a 3D backbone, a BEV backbone, and a detection head. Our contribution lies in proposing a novel 3D backbone designed to efficiently capture flexible contextual information. The key component is the UniMamba Block, which first employs a spatial locality modeling module (SLM) (Sec. 3.3.1) to capture the dynamic structure embedding, and then utilizes a complementary Z-order (Sec. 3.3.2) to convert 3D voxels into a 1D sequence. To simultaneously capture contextual information from different receptive fields, we use Local-Global Sequential Aggregator (LGSA) (Sec. 3.3.3) to encode both local and global sequences. Additionally, similar to [48], we adopt an encoder-decoder structure to stack UniMamba blocks, forming the final backbone architecture (Sec. 3.4).

## 3.3. UniMamba Block

### 3.3.1. Spatial Locality Modeling

Like other Mamba-based architectures [11, 15, 22, 50], compressing 2D/3D space into a 1D sequence inevitably results in the loss of local spatial position information. To address this issue, most methods often design various complex serialization techniques to maintain locality. However, these approaches tend to incur high computational costs and yield only limited effectiveness. Inspired by previous works [24, 42] that use sparse convolutions to provide positional information, we introduce a simple submanifold convolution as Spatial Locality Modeling module (SLM) within the UniMamba block:

$$SLM(x) = SubConv3D(x) \quad (4)$$

Here,  $SubConv3D(\cdot)$  refers to a standard 3D submanifold convolution. Thanks to the manifold design, it possesses geometric adaptability, effectively capturing local features and maintaining shape information. Therefore, we utilize it to compensate for losing local positional information.

### 3.3.2. Complementary Z-order Serialization

The purpose of serializing non-empty voxels is to find a path that traverses all input voxels. To preserve spatial



topology, the serialization of 3D voxels can be viewed as a space-filling curve process. Existing space-filling curves mainly include Hilbert [13] and Z-order [28] curves. While the Hilbert curve offers a better locality, constructing its index is computationally expensive. Thanks to the locality enhancement design (see Sec. 3.3.1), we do not heavily rely on preserving spatial topology information during serialization. Therefore, we opt for the computationally efficient Z-order curve. Specifically, given the coordinates of the input voxel set  $\mathcal{C} = \{(x_i, y_i, z_i), i \in (1, N)\}$ , where  $N$  denotes the number of voxels, the corresponding Z-order code  $\mathcal{Z}^P = \{z_i^P, i \in (1, N)\}$  is computed by the bit-interleaving function [28]. Finally, sorting the Z-order code  $\mathcal{Z}^P$  in ascending order to gain the Z-order index  $\mathcal{Z}^{index} = \{z_i^{index}, i \in (1, N)\}$  for each voxel.

Traditional Z-order curve using the X-axis as the primary order to calculate the index. However, we observe that indexing solely in the X-direction results in the preservation of spatial proximity only along the X-axis. Therefore, we introduce a variant that uses the Y-axis as the primary order for indexing.

### 3.3.3. Local-Global Sequential Aggregator

Richer global contextual information is essential for enhancing 3D detection capabilities. Utilizing Mamba’s computational advantages, treating the entire scene as a group to extract long-range global dependencies is intuitive. But the fine-grained local information is also crucial. Therefore, we propose the Local-Global Sequential Aggregator (LGSA), which models the “local and global” inter-dependencies simultaneously, as shown in Fig. 3.

**Global Sequential Encoder (GSE)** treats all non-empty voxels in the scene as a 1D sequence to directly establish a global receptive field. Unlike traditional window-based serialization, it does not create explicit local windows. The basic GSE layer includes two cascaded Mamba layers to encode the serialized voxels using Complementary Z-order. Specifically, given the input voxel sets  $\mathcal{F} \in \mathbb{R}^{N \times C}$  and their corresponding voxel coordinates sets  $\mathcal{C} \in \mathbb{R}^{N \times 3}$ , We first serialize  $\mathcal{F}$  using X-axis Z-order to obtain the corresponding voxel sequence  $\mathcal{F}^X$  and coordinates  $\mathcal{C}^X$ . Subsequently, the reordered sequence  $\mathcal{F}^X$  is input into the first Mamba layer to obtain the output  $\mathcal{F}_{out}^X$ . After that, the sequence  $\mathcal{F}_{out}^X$  is reordered using the Y-axis Z-order curve to obtain the voxel sequence  $\mathcal{F}^Y$  and coordinates  $\mathcal{C}^Y$  and input into the second Mamba layer to produce the output  $\mathcal{F}^G$  of the GSE. The specific calculations can be summarized as follows:

$$\begin{aligned} \mathcal{F}^X, \mathcal{C}^X &= \text{Z\_INDEX\_X}(\mathcal{F}, \mathcal{C}), \\ \mathcal{F}_{out}^X &= \text{MAMBA}_1(\mathcal{F}^X), \\ \mathcal{F}^Y, \mathcal{C}^Y &= \text{Z\_INDEX\_Y}(\mathcal{F}_{out}^X, \mathcal{C}^X), \\ \mathcal{F}^G &= \text{MAMBA}_2(\mathcal{F}^Y) \end{aligned} \quad (5)$$

where In this context,  $\text{Z\_INDEX\_X}(\cdot)$  and  $\text{Z\_INDEX\_Y}(\cdot)$  represent the Z-order curve indexing functions for the X-axis and Y-axis, respectively.  $\text{MAMBA}_i(\cdot)$  refers to the  $i$ th basic Mamba layer in the GSE, where the input dimension is  $C$ .  $\mathcal{F}_{out}^G \in \mathbb{R}^{N \times C}$  is the output of the GSE.

**Local Sequential Encoder (LSE).** Unlike GSE, LSE is a window-based grouping architecture. Following the traditional window partitioning method [7, 40] based on transformers, We divide all the voxels into non-overlapping 3D windows. However, unlike the previous sequential traversal of windows, we apply the Z-order curve for traversal within the local windows. Specifically, given a window size of  $(w_x, w_y, w_z)$ , for each voxel  $v_i$ , we can compute its window coordinates  $c_{win} = (\lfloor x_i/w_x \rfloor, \lfloor y_i/w_y \rfloor, \lfloor z_i/w_z \rfloor)$  and its local coordinates within window  $c_{local} = (x_i - \lfloor x/w_x \rfloor \cdot w_x, y_i - \lfloor y/w_y \rfloor \cdot w_y, z_i - \lfloor z/w_z \rfloor \cdot w_z)$ . Then, we use the local window coordinates  $c_{local}$  as input for the Z-order to obtain the voxel index within the local window. To enhance efficiency, we adopt the grouping method consistent with FlatFormer [23]. After windows-based grouping, we partition  $\mathcal{F}$  into multiple equal-length 1D sequences, denoted as  $\mathcal{F}_{local} = \{f_i, i \in [1, \lceil N/L \rceil]\}$ , where  $L$  denotes the group size. The calculation of LSE is as follows:

$$\begin{aligned} f_{ilocal}^X, c_{ilocal}^X &= \text{Z\_INDEX\_X}(f_{local}, c_{local}), \\ f_{ilocal}^X &= \text{MAMBA}_1(f_{ilocal}^X), \\ f_{ilocal}^Y, c_{ilocal}^Y &= \text{Z\_INDEX\_Y}(f_{ilocal}^X, c_{ilocal}^X), \\ f_{ilocal}^L &= \text{MAMBA}_2(f_{ilocal}^Y), \\ F^L &= \text{Concat}(f_{1out}^L, \dots, f_{\lceil N/L \rceil out}^L) \end{aligned} \quad (6)$$

**Local-Global Aggregation.** To simultaneously extract local details and global context for each voxel, We adopt a channel grouping strategy to aggregate features with different receptive fields. For the input  $\mathcal{F} \in \mathbb{R}^{N \times C}$ , we divide it into  $M$  groups along the channel dimension, obtaining a set of voxel feature collections  $\mathcal{F} = \{F_i \in \mathbb{R}^{N \times c}, i \in [1, M]\}$ , where each group has a channel dimension of  $c = C/M$ . For the first  $J$  groups, we apply GSEs for processing, while the remaining groups are processed using LSEs. Finally, we concatenate all the processed groups along the channel dimension to obtain the final output. The computation process can be expressed as follows:

$$\begin{aligned} \mathcal{F}^A &= \text{Concat}[F_1^G, \dots, F_J^G, F_{J+1}^L, \dots, F_M^L], \\ \mathcal{F}^B &= \text{LayerNorm}(\mathcal{F}^A) + \mathcal{F}^A, \\ \mathcal{F}^A &= \text{LayerNorm}(\text{FFN}(\mathcal{F}^B) + \mathcal{F}^B) \end{aligned} \quad (7)$$

Where  $\text{FFN}(x) = \text{Linear}(\text{Relu}(\text{Linear}(x)))$  is a standard feedforward neural network, which is used to capture the feature interactions between different receptive fields.

## 3.4. The UniMamba 3D Backbone

With the proposed UniMamba Block, we build UniMamba 3D Backbone with flexible receptive fields and great spatial

Table 1. Comparison experiments on the nuScenes without using any test-time augmentation and model ensemble strategies. ‘C.V.’, ‘Ped.’, ‘Motor.’, ‘B.C.’, and ‘T.C.’ represent construction vehicle, pedestrian, motorcycle, bicycle and traffic cone, respectively.

Method	Present at	mAP	NDS	Car	Truck	Bus	Trailer	C.V.	Ped.	Motor.	B.C.	T.C.	Barrier
Results on the val set													
CenterPoint [47]	CVPR’2021	59.2	66.5	84.9	57.4	70.7	38.1	16.9	85.1	59.0	42.0	69.8	68.3
Transfusion-L [1]	CVPR’2022	65.5	70.1	86.9	60.8	73.1	43.4	25.2	87.5	72.9	57.3	77.2	70.3
VoxelNeXt [5]	CVPR’2023	60.5	66.7	83.9	55.5	70.5	38.1	21.1	84.6	62.8	50.0	69.4	69.4
SAFDNet [49]	CVPR’2024	66.3	71.0	87.6	60.8	78.0	43.5	26.6	87.8	75.5	58.0	75.0	69.7
SEED [25]	ECCV’2024	66.2	71.2	-	-	-	-	-	-	-	-	-	-
LION-Mamba [24]	NIPS’2024	68.0	72.1	87.9	<b>64.9</b>	77.6	44.4	28.5	89.6	<b>75.6</b>	<b>59.4</b>	<b>80.8</b>	71.6
UniMamba (Ours)	-	<b>68.5</b>	<b>72.6</b>	<b>88.7</b>	<b>64.7</b>	<b>79.7</b>	<b>47.9</b>	<b>28.7</b>	<b>89.7</b>	<b>74.6</b>	<b>59.1</b>	<b>79.5</b>	<b>72.3</b>
Results on the test set													
3DSSD [46]	CVPR’2020	42.6	56.4	81.2	47.2	61.4	30.5	12.6	70.2	36.0	8.6	31.1	47.9
PillarNet [32]	ECCV’2022	66.0	71.4	87.6	57.5	63.6	63.1	27.9	87.3	70.1	42.3	83.3	77.2
Focals Conv [3]	CVPR’2022	63.8	70.0	86.7	56.3	67.7	59.5	23.8	87.5	64.5	36.3	81.4	74.1
LargeKernel3D [4]	CVPR’2023	65.4	70.6	85.5	53.8	64.4	59.5	29.7	85.9	72.7	46.8	79.9	75.5
DSVT [40]	CVPR’2023	68.4	72.7	86.8	58.4	67.3	63.1	<b>37.1</b>	88.0	73.0	47.2	84.9	78.4
HEDNet [48]	NIPS’2023	67.7	72.0	87.1	56.5	70.0	63.5	33.6	87.9	70.4	44.8	85.1	78.1
SAFDNet [49]	CVPR’2024	68.3	72.3	87.3	57.3	68.0	63.7	37.3	89.0	71.1	44.8	84.9	<b>79.5</b>
UniMamba (Ours)	-	<b>70.2</b>	<b>74.0</b>	<b>87.9</b>	<b>60.4</b>	<b>70.9</b>	<b>65.9</b>	36.7	<b>90.5</b>	<b>73.5</b>	<b>49.5</b>	<b>86.9</b>	79.4

modeling capacity. The architecture of UniMamba is shown in Fig. 2. Following [48], we use an encoder-decoder architecture to stack UniMamba Blocks for further hierarchical feature extraction. As a general voxel-based 3D backbone, we replace the backbone in LION [24] to construct our detector. For Argoverse 2 [41], we build on SAFDNet [49]. The configuration of the detection head and loss functions remains consistent with the baseline.

## 4. Experiments

### 4.1. Datasets and Metrics

**nuScenes** [2] is a sophisticated outdoor dataset comprising 1,000 scenarios, with 700 allocated for training, 150 for validation, and 150 for testing. It encompasses a diverse array of object annotations across 10 categories, representing the majority of traffic participants. The size of objects varies significantly among these categories, which poses considerable challenges for detection. We evaluate the effectiveness of our approach using the provided assessment tools, and reporting metrics including NDS and mAP.

**Waymo Open Dataset (WOD)** [37] is a large-scale dataset comprising 798 training scenarios and 202 validation scenarios, with 160,000 and 40,000 samples, respectively. To assess detection performance, the dataset toolkit provides metrics that include mean Average Precision (mAP) and mAPH, where mAPH is the mean average precision weighted by heading. There are two levels of detection difficulty defined based on the density of points within the bounding box: LEVEL\_1 (L1) includes bounding boxes with more than five points, while LEVEL\_2 (L2) encompasses bounding boxes containing one to five points.

**Argoverse 2** [41] is a highly challenging dataset. It has

an ultra-long detection range ( $200m \times 200m$ ) and includes annotations for 26 different types of objects, posing significant challenges for both the real-time performance and detection capabilities. The dataset comprises a total of 1,000 scene sequences, with 700 designated for training and 150 for testing. We follow previous methods [9] by using mean Average Precision (mAP) to evaluate performance.

### 4.2. Implementation Details

We implement our UniMamba based on LION [24]. Following previous methods, we use voxel sizes of  $(0.3m, 0.3m, 0.25m)$ ,  $(0.32m, 0.32m, 0.1875m)$ , and  $(0.4m, 0.4m, 0.25m)$  for voxelization of the nuScenes, Waymo, and Argoverse 2 datasets, respectively, where the number of voxel feature channels is set to 128. The downsampling stride for encoder-decoder is set to  $\{1, 2, 2\}$ , with each scale containing 1 layer of UniMamba Block. For each UniMamba block, the number of channel groups  $M$  is set to 4, with  $J = 2$  groups applying GSE and the remaining two applying LSE. The other training hyperparameters are configured consistently with [24]. All experiments are conducted using 8 Tesla A800 GPUs, utilizing the AdamW [26] optimizer. For more network details, please refer to the appendix.

### 4.3. Comparison Experiments

**Result on nusenes** As shown in Tab. 1, our UniMamba demonstrates a significant performance improvement on the NuScenes dataset, being the first lidar-based method to exceed 70 mAP on the test set. Compared to the traditional SpCNN-based state-of-the-art SAFDNet [49], it achieves *improvements of 2.2 mAP and 1.6 NDS*. Additionally, when compared to the transformer-based method DSVT [40],

Table 2. Comparison experiments on the Waymo Open validation set. All of these models are trained with single-frame inputs and no additional test-time augmentation. ‘‘Ped.’’ denotes Pedestrian, and ‘‘Cyc.’’ denotes Cyclist.

Method	Present at	Vehicle(L1) AP/APH	Vehicle(L2) AP/APH	Ped.(L1) AP/APH	Ped.(L2) AP/APH	Cyc.(L1) AP/APH	Cyc.(L2) AP/APH	ALL (L2) mAP/mAPH
PointPillar [16]	CVPR’2019	70.43/69.83	62.18/61.64	66.21/46.32	58.18/40.64	55.26/51.75	53.18/49.80	57.85/50.69
SECOND [44]	Sensors’2018	70.96/70.34	62.58/62.02	65.23/54.24	57.22/47.49	57.13/55.62	54.97/53.53	58.26/54.35
CenterPoint [47]	CVPR’2021	74.20/73.60	66.20/65.70	76.60/70.50	68.80/63.20	72.30/71.10	69.70/68.50	68.20/65.80
Voxset [12]	CVPR’2022	74.50/74.00	66.00/65.60	80.00/72.40	72.50/65.40	71.60/70.30	69.00/67.70	69.17/66.23
SST [7]	CVPR’2022	75.13/74.64	66.61/66.17	80.07/72.12	72.38/65.01	71.49/70.20	68.85/67.61	69.28/66.26
AFDetV2 [14]	AAAI’2022	77.64/77.14	69.68/69.22	80.19/72.62	72.16/66.95	73.72/72.74	71.06/70.12	70.97/68.76
PillarNet [32]	ECCV’2022	79.09/78.59	70.92/70.46	80.59/74.01	72.28/66.17	72.29/71.21	69.72/68.67	70.97/68.43
PV_RCNN++ [34]	IJCV’2023	79.25/78.78	70.61/70.18	81.83/76.28	73.17/68.00	73.72/72.66	71.21/70.19	71.66/69.46
OcTr [52]	CVPR’2023	79.20/78.70	70.80/70.40	82.20/76.30	74.00/68.50	73.90/72.80	71.10/69.20	71.97/69.37
FlatFormer [23]	CVPR’2023	- / -	69.00/68.60	- / -	71.50/65.30	- / -	68.60/67.50	69.70/67.13
DSVT-V [40]	CVPR’2023	79.70/79.30	71.40/71.00	83.70/78.90	76.10/71.50	77.50/76.50	74.60/73.70	74.00/72.10
MsSVT++ [17]	TPAMI’2023	78.96/78.39	70.57/70.01	80.64/73.78	73.12/66.80	75.98/74.73	72.97/71.82	72.22/69.54
HEDNet [48]	NIPS’2023	<b>81.10/80.60</b>	<b>73.20/72.70</b>	84.40/80.00	76.80/72.60	78.70/77.70	75.80/74.90	75.30/73.40
SEED-B [25]	ECCV’2024	79.70/79.20	71.80/71.40	83.10/78.30	75.50/70.80	80.00/78.80	77.30/76.10	74.87/72.77
VoxelMamba [50]	NIPS’2024	80.80/80.30	72.60/72.20	85.00/80.80	77.70/73.60	78.60/77.60	75.70/74.80	75.33/73.53
LION-Mamba-L [24]	NIPS’2024	80.30/79.90	72.00/71.60	<b>85.80/81.40</b>	<b>78.50/74.30</b>	80.10/79.00	77.20/76.20	75.90/74.00
UniMamba (Ours)	-	80.60/80.06	72.28/71.77	<b>85.99/81.25</b>	<b>78.66/74.07</b>	<b>80.33/79.30</b>	<b>77.46/76.48</b>	<b>76.13/74.11</b>

Table 3. Comparison experiments on the Argoverse 2 val set. Here, C-Barrel, MPC-Sign, A-Bus, C-Cone, V-Trailer, MBT, W-Device, and W-Rider refer to Construction Barrel, Mobile Pedestrian Crossing Sign, Articulated Bus, Construction Cone, Vehicular Trailer, Message Board Trailer, Wheeled Device, and Wheeled Rider, respectively.

Method	mAP	Vehicle	Bus	Pedestrian	Stop Sign	Box Truck	Bollard	C-Barrel	Motorcyclist	MPC-Sign	Motorcycle	Bicycle	A-Bus	School Bus	Truck	Truck Cab	C-Cone	V-Trailer	Sign	Large Vehicle	Stroller	Bicyclist	MBT	Dog	Wheelchair	W-Device	W-Rider
CenterPoint [47]	22.0	67.6	38.9	46.5	16.9	37.4	40.1	32.2	28.6	27.4	33.4	24.5	8.7	25.8	22.1	22.6	29.5	22.4	6.3	3.9	0.5	20.1	0.0	3.9	0.5	10.9	4.2
FSDv1 [8]	28.2	68.1	40.9	59.0	29.0	38.5	41.8	42.6	39.7	26.2	49.0	38.6	20.4	30.5	21.1	14.8	41.2	26.9	11.9	5.9	13.8	33.4	0.0	9.5	7.1	14.0	9.2
VoxelNeXt [5]	30.7	72.7	38.8	63.2	40.2	40.1	53.9	64.9	44.7	39.4	42.4	40.6	20.1	25.2	16.9	19.9	44.9	20.9	14.9	6.8	15.7	32.4	0.0	14.4	0.1	17.4	6.6
HEDNet [48]	37.1	78.2	47.7	67.6	46.4	45.9	56.9	67.0	48.7	46.5	58.2	47.5	23.3	40.9	21.6	27.5	46.8	27.9	20.6	6.9	27.2	38.7	0.0	30.7	9.5	28.5	8.7
FSDv2 [9]	37.6	77.0	47.6	70.5	43.6	41.5	53.9	58.5	56.8	39.0	60.7	49.4	28.4	41.9	24.0	<b>30.2</b>	44.9	<b>33.4</b>	16.6	7.3	32.5	45.9	<b>1.0</b>	12.6	<b>17.1</b>	26.3	<b>17.2</b>
SAFDNet [49]	39.7	78.5	<b>49.4</b>	70.7	51.5	44.7	65.7	72.3	54.3	49.7	60.8	50.0	<b>31.3</b>	<b>44.9</b>	23.6	24.7	55.4	31.4	22.1	7.1	31.1	42.7	0.0	26.1	1.4	30.2	11.5
LION-Mamba [24]	41.5	75.1	43.6	73.9	<b>53.9</b>	45.1	66.4	74.7	<b>61.3</b>	48.7	<b>65.1</b>	<b>56.2</b>	21.7	42.7	19.0	25.3	58.4	28.9	<b>23.6</b>	<b>8.3</b>	<b>49.5</b>	47.3	0.0	<b>31.4</b>	8.7	<b>37.6</b>	11.8
UniMamba (Ours)	<b>42.0</b>	<b>78.9</b>	47.9	<b>74.3</b>	51.8	<b>46.8</b>	<b>67.8</b>	<b>76.9</b>	55.8	<b>51.7</b>	62.8	52.2	30.2	44.6	<b>24.6</b>	28.1	<b>59.4</b>	32.2	23.2	6.7	41.5	<b>48.5</b>	0.0	26.4	8.1	36.4	13.7

UniMamba shows enhancements of 1.8 mAP and 1.3 NDS. This validates the suitability of the Mamba architecture as a 3D backbone. Notably, UniMamba has significantly improved detection performance for various object sizes, achieving a 3.9 mAP increase for Truck (large target) and a 1.9 mAP improvement for Pedestrian (small target). This highlights the effectiveness of UniMamba’s hybrid architecture design and flexible receptive field.

**Result on Waymo** We then compare UniMamba with previous methods on the Waymo dataset, establishing a new state-of-the-art. As shown in Tab. 2, our method outperforms the previous best SpCNN-based method, HEDNet [48], by 0.83 in L2\_mAP. Notably, compared to the Transformer-based method DSVT [40], UniMamba has demonstrated significant advantages in small object, achieving improvements of +2.56 L2\_mAP for pedestrian and +2.86 L2\_mAP for cyclist. This emphasizes the critical importance of local details for the perception of small targets.

**Result on Argoverse 2** We also evaluated UniMamba on the Argoverse 2 dataset, which has a larger detection range, with results shown in Tab. 3. UniMamba achieved state-of-the-art performance, reaching 42.0 mAP. Compared to

Table 4. Ablation Study of Spatial Locality Modeling module cross Serializations. For a fair comparison, the latency is calculated as the time taken to serialize 20,000 input voxels.

Serialization Method	w/o SLM		w/ SLM		Latency
	mAP	NDS	mAP	NDS	
Random	66.2	70.9	67.4	71.5	-
Hilbert	67.4	71.7	67.6	71.8	15.8 ms
Z-order	67.2	71.5	67.6	71.7	0.9 ms
Complementary Z-order	67.6	71.9	<b>67.9</b>	<b>72.0</b>	<b>0.9 ms</b>

the previous state-of-the-art SAFDNet [49], our method achieved an improvement of 2.3 mAP, by simply replacing its 3D backbone. This demonstrates the powerful 3D feature extraction capability of UniMamba.

#### 4.4. Ablation Study

**Effect of Spatial Locality Modeling.** To validate the effectiveness of the proposed SLM in mitigating the loss of spatial locality, we compare it with several popular space-filling curves. The ‘‘Random’’ refers to the configuration where no spatial curve is applied. As shown in rows 2-4 of Tab. 4, when neither SLM nor any spatial curve is used,

Table 5. Ablation Study of the Number of Channel Groups in LGSA. We use Transfusion-L [1] as the baseline.

Channel Groups	GSE	LSE	mAP NDS	
1 (Baseline)	0	0	65.7	70.5
1 (LSE only)	0	1	67.7	72.0
1 (GSE only)	1	0	67.8	72.2
2	1	1	68.4	72.5
4	2	2	<b>68.5</b>	<b>72.6</b>
4	1	3	68.4	72.5
4	3	1	68.3	72.2
8	4	4	68.2	72.3

performance drops significantly (- 1.4 mAP), demonstrating the importance of spatial locality. Compared with the standard Z-order curve, the Hilbert curve which better preserves locality shows a 0.2 mAP advantage. With SLM, the "Random" achieves 67.4 mAP, comparable to the performance with space-filling curves. Additionally, the Z-order curve achieves performance parity with the Hilbert curve (67.6 mAP) but requires only 1/17 time cost. These results demonstrate the effectiveness of Spatial Locality Modeling in capturing the dynamic structure embedding.

**Effect of Complementary Z-order Serialization.** As shown in row 5 of Tab. 4, Compared to the single-direction Z-order curve, using the Complementary Z-order curve brings a 0.3 mAP improvement. This demonstrates the effectiveness of using z-order for serialization from two directions to further enhance locality.

**Effect of Design Choices in LGSA.** We study the effect of LSE and GSE proposed in LGSA compared with the SpCNN-based method [1]. Experimental results are shown in rows 2-4 of Tab. 5, which indicate that the SSM-based architecture offers significant advantages, surpassing the baseline by 2.0 mAP. This confirms the effectiveness of our proposed LSE and GSE.

**Number of Channel Groups in LGSA.** As shown in rows 4-8 of Tab. 5, we conduct an ablation study on the number of channel groups and the quantities of LSE and GSE. It can be observed that using only two channel groups leads to a significant performance improvement (+0.6 mAP), which demonstrates the importance of simultaneously modeling both local and global receptive fields. The performance is optimal when the number of groups increases to 4. However, when using an imbalanced LSE and GSE, there is a decline in performance, indicating that LSE and GSE hold equal importance for subsequent detection tasks.

**Different Local-Global Feature Aggregation Methods.** To validate the effectiveness of the channel grouping strategy in aggregating local-global contextual information, we compare it with both sequential " $LSE - GSE$ " and parallel " $LSE \oplus GSE$ " approaches without channel grouping. As shown in Tab. 6, the channel grouping strategy achieves

Table 6. Different Local-Global Feature Aggregation Methods.

Method	mAP	NDS	Latency
Sequential	68.0	72.3	158.9ms
Parallel	68.4	72.5	162.7ms
<b>Channel Group (Ours)</b>	<b>68.5</b>	<b>72.6</b>	<b>121.4ms</b>

Table 7. Comparison of computational costs and parameters of different backbone architectures

Method	Backbone	L2 mAP/mAPH	Flops	Params
CenterPoint	SpCNN	68.20/65.80	48.5G	2.7M
FlatFormer	Transformer	69.70/67.13	<b>48.5G</b>	<b>1.1M</b>
DSVT-V		74.00/72.10	110.2G	2.7M
<b>UniMamba</b>	<b>Mamba</b>	<b>75.40/73.61</b>	61.9G	1.6M

the best performance without introducing additional time overhead. This demonstrates the effectiveness of adaptively capturing multiple receptive fields between channel groups.

**Efficiency Analysis.** To validate the computational efficiency of UniMamba, we compare it with mainstream 3D backbones based on SpCNN and Transformer. As shown in Tab. 7, UniMamba achieved an L2\_mAP performance of 75.40 with a computational load of 61.9 GFlops. Compared to DSVT, UniMamba improves the L2\_mAP by 1.4 while operating at approximately half the computational cost. These results demonstrate that UniMamba maintains strong detection accuracy with relatively low computational costs and parameter sizes.

## 5. Conclusion

In this paper, we propose a novel unified Mamba architecture, UniMamba, to integrate 3D convolution and State Space Models (SSM) in a concise multi-head format. UniMamba offers flexible receptive fields and excellent spatial modeling capabilities. We first analyze the challenges of directly applying the Mamba architecture in Lidar-based 3D detection tasks, including locality loss and limited spatial diversity, which restrict its ability to capture complex local and global dependencies. Then, we introduce a spatial locality modeling module to capture dynamic structural embeddings and use complementary Z-order curves to preserve spatial proximity when transforming 3D voxels into a 1D sequence. Our core contribution is the Local-Global Sequential Aggregator (LSGA), which includes a Local Sequential Encoder and Global Sequential Encoder to capture local and global receptive fields. Additionally, we adopt a channel-grouping strategy to efficiently aggregate these various receptive fields. Experiments on three challenging datasets (nuScenes, Waymo and Argoverse 2) demonstrate the superior performance of our UniMamba.



## References

- [1] Xuyang Bai, Zeyu Hu, Xinge Zhu, Qingqiu Huang, Yilun Chen, Hongbo Fu, and Chiew-Lan Tai. Transfusion: Robust lidar-camera fusion for 3d object detection with transformers. In *Proceedings of the IEEE/CVF conference on computer vision and pattern recognition*, pages 1090–1099, 2022. 2, 6, 8
- [2] Holger Caesar, Varun Bankiti, Alex H. Lang, Sourabh Vora, Venice Erin Liong, Qiang Xu, Anush Krishnan, Yu Pan, Giancarlo Baldan, and Oscar Beijbom. nuscenes: A multi-modal dataset for autonomous driving. In *CVPR*, 2020. 6, 1
- [3] Yukang Chen, Yanwei Li, Xiangyu Zhang, Jian Sun, and Jiaya Jia. Focal sparse convolutional networks for 3d object detection. In *Proceedings of the IEEE/CVF Conference on Computer Vision and Pattern Recognition*, pages 5428–5437, 2022. 2, 6
- [4] Yukang Chen, Jianhui Liu, Xiangyu Zhang, Xiaojuan Qi, and Jiaya Jia. Largekernel3d: Scaling up kernels in 3d sparse cnns. In *Proceedings of the IEEE/CVF Conference on Computer Vision and Pattern Recognition*, pages 13488–13498, 2023. 1, 2, 6
- [5] Yukang Chen, Jianhui Liu, Xiangyu Zhang, Xiaojuan Qi, and Jiaya Jia. Voxelnxt: Fully sparse voxelnet for 3d object detection and tracking. In *Proceedings of the IEEE/CVF Conference on Computer Vision and Pattern Recognition*, pages 21674–21683, 2023. 2, 6, 7
- [6] Jiajun Deng, Shaoshuai Shi, Peiwei Li, Wengang Zhou, Yanyong Zhang, and Houqiang Li. Voxel r-cnn: Towards high performance voxel-based 3d object detection. In *Proceedings of the AAAI Conference on Artificial Intelligence*, pages 1201–1209, 2021. 2
- [7] Lue Fan, Ziqi Pang, Tianyuan Zhang, Yu-Xiong Wang, Hang Zhao, Feng Wang, Naiyan Wang, and Zhaoxiang Zhang. Embracing single stride 3d object detector with sparse transformer. In *Proceedings of the IEEE/CVF conference on computer vision and pattern recognition*, pages 8458–8468, 2022. 3, 5, 7
- [8] Lue Fan, Feng Wang, Naiyan Wang, and ZHAO-XIANG ZHANG. Fully sparse 3d object detection. *Advances in Neural Information Processing Systems*, 35:351–363, 2022. 7
- [9] Lue Fan, Feng Wang, Naiyan Wang, and Zhaoxiang Zhang. Fsd v2: Improving fully sparse 3d object detection with virtual voxels. *arXiv preprint arXiv:2308.03755*, 2023. 6, 7
- [10] Albert Gu and Tri Dao. Mamba: Linear-time sequence modeling with selective state spaces. *arXiv preprint arXiv:2312.00752*, 2023. 2, 3
- [11] Xu Han, Yuan Tang, Zhaoxuan Wang, and Xianzhi Li. Mamba3d: Enhancing local features for 3d point cloud analysis via state space model. *arXiv preprint arXiv:2404.14966*, 2024. 3, 4
- [12] Chenhang He, Ruihuang Li, Shuai Li, and Lei Zhang. Voxel set transformer: A set-to-set approach to 3d object detection from point clouds. In *Proceedings of the IEEE/CVF Conference on Computer Vision and Pattern Recognition*, pages 8417–8427, 2022. 7
- [13] David Hilbert. *Über die stetige Abbildung einer Linie auf ein Flächenstück*, page 1–2. 5
- [14] Yihan Hu, Zhuangzhuang Ding, Runzhou Ge, Wenxin Shao, Li Huang, Kun Li, and Qiang Liu. Afdetv2: Rethinking the necessity of the second stage for object detection from point clouds. In *Proceedings of the AAAI Conference on Artificial Intelligence*, pages 969–979, 2022. 7
- [15] Tao Huang, Xiaohuan Pei, Shan You, Fei Wang, Chen Qian, and Chang Xu. Localmamba: Visual state space model with windowed selective scan. *arXiv preprint arXiv:2403.09338*, 2024. 3, 4
- [16] Alex H Lang, Sourabh Vora, Holger Caesar, Lubing Zhou, Jiong Yang, and Oscar Beijbom. Pointpillars: Fast encoders for object detection from point clouds. In *Proceedings of the IEEE/CVF conference on computer vision and pattern recognition*, pages 12697–12705, 2019. 7
- [17] Jianan Li, Shaocong Dong, Lihe Ding, and Tingfa Xu. Mssvt++: Mixed-scale sparse voxel transformer with center voting for 3d object detection. *IEEE Transactions on Pattern Analysis and Machine Intelligence*, pages 1–17, 2023. 7
- [18] Kunchang Li, Yali Wang, Peng Gao, Guanglu Song, Yu Liu, Hongsheng Li, and Yu Qiao. Uniformer: Unified transformer for efficient spatiotemporal representation learning. *arXiv preprint arXiv:2201.04676*, 2022. 2
- [19] Kunchang Li, Yali Wang, Yanan He, Yizhuo Li, Yi Wang, Limin Wang, and Yu Qiao. Uniformerv2: Spatiotemporal learning by arming image vits with video uniformer, 2022. 2
- [20] Kunchang Li, Xinhao Li, Yi Wang, Yanan He, Yali Wang, Limin Wang, and Yu Qiao. Videomamba: State space model for efficient video understanding. In *European Conference on Computer Vision*, pages 237–255. Springer, 2024. 3
- [21] Dingkan Liang, Xin Zhou, Wei Xu, Xingkui Zhu, Zhikang Zou, Xiaoqing Ye, Xiao Tan, and Xiang Bai. Pointmamba: A simple state space model for point cloud analysis. In *Advances in Neural Information Processing Systems*, 2024.
- [22] Yue Liu, Yunjie Tian, Yuzhong Zhao, Hongtian Yu, Lingxi Xie, Yaowei Wang, Qixiang Ye, and Yunfan Liu. Vmamba: Visual state space model. *arXiv preprint arXiv:2401.10166*, 2024. 2, 3, 4
- [23] Zhijian Liu, Xinyu Yang, Haotian Tang, Shang Yang, and Song Han. FlatFormer: Flattened window attention for efficient point cloud transformer. In *IEEE/CVF Conference on Computer Vision and Pattern Recognition (CVPR)*, 2023. 2, 3, 5, 7, 1
- [24] Zhe Liu, Jinghua Hou, Xinyu Wang, Xiaoqing Ye, Jingdong Wang, Hengshuang Zhao, and Xiang Bai. Lion: Linear group rnn for 3d object detection in point clouds. *Advances in Neural Information Processing Systems*, 37:13601–13626, 2024. 2, 3, 4, 6, 7
- [25] Zhe Liu, Jinghua Hou, Xiaoqing Ye, Tong Wang, Jingdong Wang, and Xiang Bai. Seed: A simple and effective 3d detr in point clouds. In *European Conference on Computer Vision*, pages 110–126. Springer, 2025. 6, 7
- [26] Ilya Loshchilov and Frank Hutter. Decoupled weight decay regularization. *arXiv preprint arXiv:1711.05101*, 2017. 6
- [27] Jiageng Mao, Yujing Xue, Minzhe Niu, Haoyue Bai, Jiashi Feng, Xiaodan Liang, Hang Xu, and Chunjing Xu. Voxel

- transformer for 3d object detection. In *Proceedings of the IEEE/CVF International Conference on Computer Vision*, pages 3164–3173, 2021. 2
- [28] Jack A. Orenstein. Spatial query processing in an object-oriented database system. *ACM SIGMOD Record*, 15(2): 326–336, 1986. 5
- [29] Charles R Qi, Hao Su, Kaichun Mo, and Leonidas J Guibas. Pointnet: Deep learning on point sets for 3d classification and segmentation. In *Proceedings of the IEEE conference on computer vision and pattern recognition*, pages 652–660, 2017. 1, 2
- [30] Charles Ruizhongtai Qi, Li Yi, Hao Su, and Leonidas J Guibas. Pointnet++: Deep hierarchical feature learning on point sets in a metric space. *Advances in neural information processing systems*, 30, 2017. 1, 2
- [31] Zhiwu Qing, Haisheng Su, Weihao Gan, Dongliang Wang, Wei Wu, Xiang Wang, Yu Qiao, Junjie Yan, Changxin Gao, and Nong Sang. Temporal context aggregation network for temporal action proposal refinement. In *Proceedings of the IEEE/CVF conference on computer vision and pattern recognition*, pages 485–494, 2021. 2
- [32] Guangsheng Shi, Ruifeng Li, and Chao Ma. Pillarnet: Real-time and high-performance pillar-based 3d object detection. In *European Conference on Computer Vision*, pages 35–52. Springer, 2022. 6, 7
- [33] Shaoshuai Shi, Xiaogang Wang, and Hongsheng Li. Pointcnn: 3d object proposal generation and detection from point cloud. In *Proceedings of the IEEE/CVF conference on computer vision and pattern recognition*, pages 770–779, 2019. 1, 2
- [34] Shaoshuai Shi, Li Jiang, Jiajun Deng, Zhe Wang, Chaoxu Guo, Jianping Shi, Xiaogang Wang, and Hongsheng Li. Pvrnn++: Point-voxel feature set abstraction with local vector representation for 3d object detection. *International Journal of Computer Vision*, 131(2):531–551, 2023. 7
- [35] Haisheng Su, Feixiang Song, Cong Ma, Wei Wu, and Junchi Yan. Robosense: Large-scale dataset and benchmark for ego-centric robot perception and navigation in crowded and unstructured environments. *arXiv preprint arXiv:2408.15503*, 2024. 1
- [36] Haisheng Su, Wei Wu, and Junchi Yan. Difsd: Ego-centric fully sparse paradigm with uncertainty denoising and iterative refinement for efficient end-to-end autonomous driving. *arXiv preprint arXiv:2409.09777*, 2024. 1
- [37] Pei Sun, Henrik Kretzschmar, Xerxes Dotiwalla, Aurelien Chouard, Vijaysai Patnaik, Paul Tsui, James Guo, Yin Zhou, Yuning Chai, Benjamin Caine, et al. Scalability in perception for autonomous driving: Waymo open dataset. In *Proceedings of the IEEE/CVF conference on computer vision and pattern recognition*, pages 2446–2454, 2020. 6, 1
- [38] Pei Sun, Mingxing Tan, Weiyue Wang, Chenxi Liu, Fei Xia, Zhaoqi Leng, and Dragomir Anguelov. Swformer: Sparse window transformer for 3d object detection in point clouds. In *European Conference on Computer Vision*, pages 426–442. Springer, 2022. 3
- [39] Ashish Vaswani, Noam Shazeer, Niki Parmar, Jakob Uszkoreit, Llion Jones, Aidan N Gomez, Łukasz Kaiser, and Illia Polosukhin. Attention is all you need. *Advances in neural information processing systems*, 30, 2017. 3
- [40] Haiyang Wang, Chen Shi, Shaoshuai Shi, Meng Lei, Sen Wang, Di He, Bernt Schiele, and Liwei Wang. Dsvt: Dynamic sparse voxel transformer with rotated sets. In *Proceedings of the IEEE/CVF Conference on Computer Vision and Pattern Recognition*, pages 13520–13529, 2023. 2, 3, 5, 6, 7, 1
- [41] Benjamin Wilson, William Qi, Tanmay Agarwal, John Lambert, Jagjeet Singh, Siddhesh Khandelwal, Bowen Pan, Ratnesh Kumar, Andrew Hartnett, Jhony Kaesemodel Pontes, et al. Argoverse 2: Next generation datasets for self-driving perception and forecasting. *arXiv preprint arXiv:2301.00493*, 2023. 6, 1
- [42] Xiaoyang Wu, Li Jiang, Peng-Shuai Wang, Zhijian Liu, Xihui Liu, Yu Qiao, Wanli Ouyang, Tong He, and Hengshuang Zhao. Point transformer v3: Simpler, faster, stronger. In *Proceedings of the IEEE/CVF Conference on Computer Vision and Pattern Recognition*, 2024. 4
- [43] Yicheng Xiao, Lin Song, Shaoli Huang, Jiangshan Wang, Siyu Song, Yixiao Ge, Xiu Li, and Ying Shan. Grootvl: Tree topology is all you need in state space model. *arXiv preprint arXiv:2406.02395*, 2024. 3
- [44] Yan Yan, Yuxing Mao, and Bo Li. Second: Sparsely embedded convolutional detection. *Sensors*, 18(10):3337, 2018. 1, 2, 7
- [45] Honghui Yang, Wenxiao Wang, Minghao Chen, Binbin Lin, Tong He, Hua Chen, Xiaofei He, and Wanli Ouyang. Pvt-ssd: Single-stage 3d object detector with point-voxel transformer. In *Proceedings of the IEEE/CVF Conference on Computer Vision and Pattern Recognition*, pages 13476–13487, 2023. 3
- [46] Zetong Yang, Yanan Sun, Shu Liu, and Jiaya Jia. 3dssd: Point-based 3d single stage object detector. In *Proceedings of the IEEE/CVF conference on computer vision and pattern recognition*, pages 11040–11048, 2020. 1, 2, 6
- [47] Tianwei Yin, Xingyi Zhou, and Philipp Krahenbuhl. Center-based 3d object detection and tracking. In *Proceedings of the IEEE/CVF conference on computer vision and pattern recognition*, pages 11784–11793, 2021. 2, 6, 7
- [48] Gang Zhang, Chen Junnan, Guohuan Gao, Jianmin Li, and Xiaolin Hu. HEDNet: A hierarchical encoder-decoder network for 3d object detection in point clouds. In *Thirty-seventh Conference on Neural Information Processing Systems*, 2023. 2, 4, 6, 7, 1
- [49] Gang Zhang, Junnan Chen, Guohuan Gao, Jianmin Li, Si Liu, and Xiaolin Hu. Safdnet: A simple and effective network for fully sparse 3d object detection. In *Proceedings of the IEEE/CVF Conference on Computer Vision and Pattern Recognition*, pages 14477–14486, 2024. 2, 6, 7, 1
- [50] Guowen Zhang, Lue Fan, Chenhang He, Zhen Lei, ZHAOXIANG ZHANG, and Lei Zhang. Voxel mamba: Group-free state space models for point cloud based 3d object detection. *Advances in Neural Information Processing Systems*, 37:81489–81509, 2024. 2, 3, 4, 7
- [51] Yifan Zhang, Qingyong Hu, Guoquan Xu, Yanxin Ma, Jianwei Wan, and Yulan Guo. Not all points are equal: Learning highly efficient point-based detectors for 3d lidar point

- clouds. In *Proceedings of the IEEE/CVF Conference on Computer Vision and Pattern Recognition*, pages 18953–18962, 2022. [2](#)
- [52] Chao Zhou, Yanan Zhang, Jiaxin Chen, and Di Huang. Octr: Octree-based transformer for 3d object detection. In *Proceedings of the IEEE/CVF Conference on Computer Vision and Pattern Recognition*, pages 5166–5175, 2023. [3](#), [7](#)
- [53] Yin Zhou and Oncel Tuzel. Voxelnet: End-to-end learning for point cloud based 3d object detection. In *Proceedings of the IEEE conference on computer vision and pattern recognition*, pages 4490–4499, 2018. [1](#), [2](#)
- [54] Lianghui Zhu, Bencheng Liao, Qian Zhang, Xinlong Wang, Wenyu Liu, and Xinggang Wang. Vision mamba: Efficient visual representation learning with bidirectional state space model. In *Forty-first International Conference on Machine Learning*. [2](#), [3](#)



# UniMamba: Unified Spatial-Channel Representation Learning with Group-Efficient Mamba for LiDAR-based 3D Object Detection

## Supplementary Material

In the supplementary materials, we first provide more details on the network implementation (Sec. A), followed by additional ablation experiments (Sec. B), and finally present the qualitative results (Sec. C).

### A. More Implementation Details

For the nuScenes [2], we first voxelize the point cloud with a range of  $[-54m, -54m, -5m, 54m, 54m, 3m]$  using a voxel size of  $[0.3m, 0.3m, 0.25m]$ , resulting in a voxel feature of  $[360, 360, 32]$ . We then employ a 5-stage UniMamba 3D Backbone. Each stage has a downsampling stride of  $\{1, 2, 2\}$ , with  $M = 4$  groups in the UniMamba block and  $J = 2$  LSEs. The window size for the X/Y-axis in the LSE of each stage is  $[13, 13]$ , while the Z-axis window size varies across stages as  $\{32, 16, 8, 4, 2\}$  (i.e., no subdivision of the window in the z-axis direction). To improve efficiency, we follow the Flatformer [23] approach and group the windows in an equal-length manner, with a group size of 1024. The window size in the X/Y-axis for the GSE is the size of the entire space (i.e.,  $[360, 360]$ ), and the Z-axis window size is consistent with that of the LSE. The input and output dimensions of the backbone are set to  $C = 128$ . The BEV backbone and detection head are consistent with DSVT [40].

For the Waymo Open Dataset [37] and Argoverse 2 dataset [41], we voxelize point clouds using sizes of  $[0.32m, 0.32m, 0.1875m]$  and  $[0.4m, 0.4m, 0.25m]$  within ranges of  $[-75.52m, -75.52m, -2m, 75.52m, 75.52m, 4m]$  and  $[-200m, -200m, -4m, 200m, 200m, -4m]$ , resulting in voxel features of  $[472, 472, 32]$  and  $[1000, 1000, 32]$ , respectively. The configurations of the UniMamba 3D Backbone remain consistent with those of nuScenes. For a fair comparison, we use a sparse detection head consistent with SAFDNet [49] for the Argoverse 2 dataset.

### B. More Ablation Experiments

#### B.1. Different Window and Group Size in LSE

To verify the impact of different window shapes and group sizes on performance in LSE, we conduct ablation experiments on the nuScenes dataset. The results for different window shapes are shown in rows 2-4 of Tab. 1, where it can be observed that the performance of UniMamba is insensitive to window shape. The results for different group sizes are presented in rows 5-8 of Tab. 1, indicating that

both smaller and larger group sizes lead to a decline in performance, with the best performance achieved at a group size of 1024. This is because a group that is too small results in a not enough receptive field, while a group that is too large lacks detailed local information.

Table 1. Comparisons of different window shapes and group sizes in LSE on the nuScenes *val* set. The ‘‘Window Shape’’ refers to the size of the window in the X/Y-axis, while the window size along the Z-axis is set to  $\{32, 16, 8, 4, 2\}$  for different stages as default (i.e., no subdivision of the window in the Z-axis direction).

Window Shape	Group Size	mAP $\uparrow$	NDS $\uparrow$
[9,9]	1024	68.4	72.5
[13,13]		<b>68.5</b>	<b>72.6</b>
[18,18]		68.5	72.5
[13,13]	256	68.3	72.4
	512	68.4	72.6
	1024	<b>68.5</b>	<b>72.6</b>
	2048	68.4	72.4

#### B.2. Effect of Downsampling Strides

To verify the effectiveness of extracting hierarchical features using the encoder-decoder architecture like HEDNet[48], we compare the performance of models with different downsampling strides. As shown in Tab. 2,  $\{1\}$  indicates the absence of the encoder-decoder architecture, while  $\{1, 2\}$  indicates only one downsampling. It can be observed that the mAP decreases sequentially for  $\{1\}$  and  $\{1, 2\}$ , which demonstrates that hierarchical features play a crucial role in detection tasks. Additionally, when the downsampling strides are  $\{1, 2, 4\}$  and  $\{1, 4, 4\}$ , the performance also declines, indicating that excessively large downsampling strides will result in the loss of some local details.

Table 2. Ablation study of different scales in each stage.

Down Strides	mAP $\uparrow$	NDS $\uparrow$
$\{1\}$	68.0	72.3
$\{1,2\}$	68.3	72.5
$\{1,2,2\}$	<b>68.5</b>	<b>72.6</b>
$\{1,2,4\}$	68.1	72.3
$\{1,4,4\}$	67.9	72.2



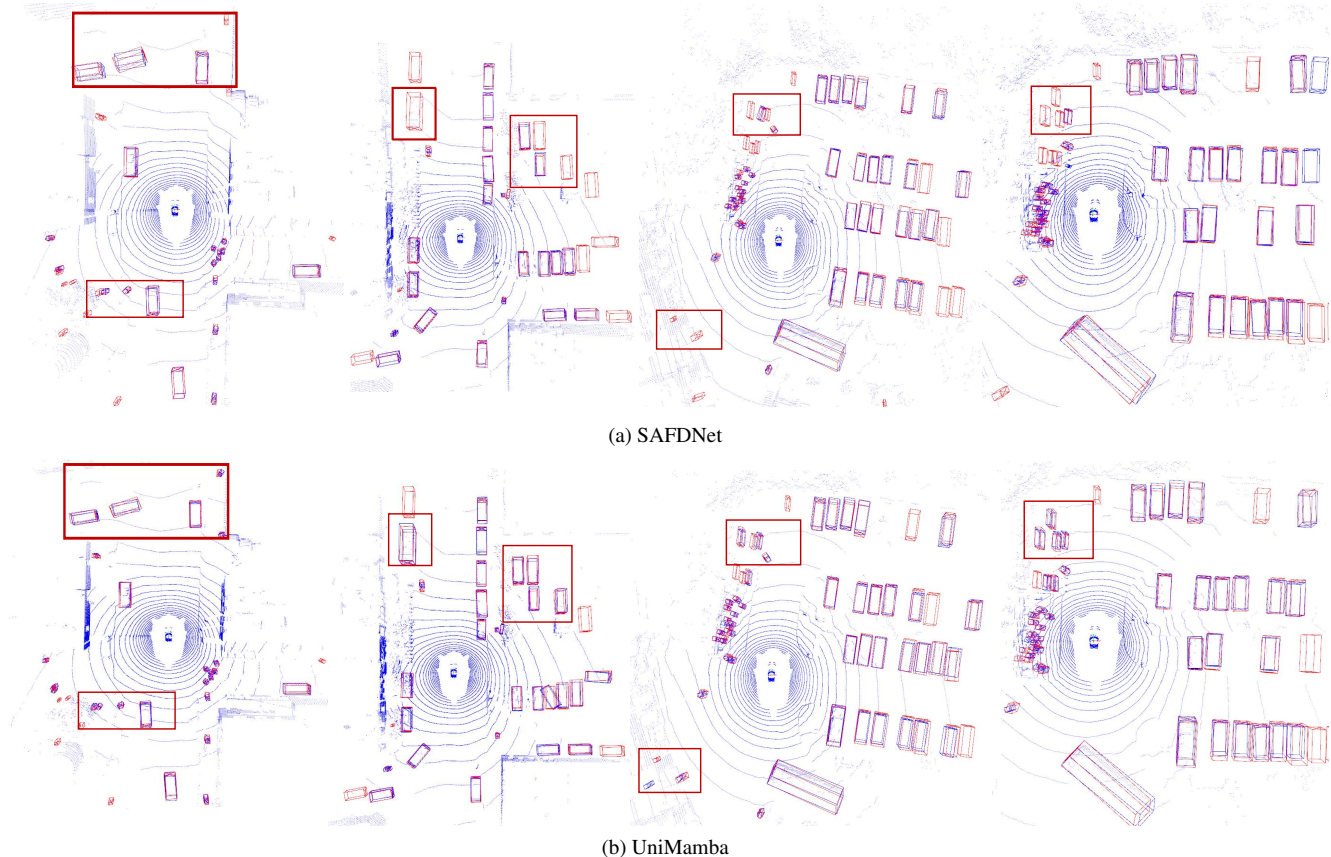


Figure 1. Visualization comparison of detection results between our UniMamba and SAFDNet [49] on the nuScenes *val* set. **Blue** indicates the prediction bounding box and **Red** indicates the ground-truth bounding box. The superior detection results are best viewed in **Red Rectangle**.

### B.3. Complementary Order in Serialization

For the Complementary Z-order, we adopt two different feature interaction methods: parallel and Sequential. The parallel method refers to separately serializing and encoding the input features in the X-direction and Y-direction, and then summing them. In contrast, the Sequential method involves first serializing and encoding the input features in the X-direction, and then performing Y-direction serializing and encoding on the encoded features. The results are shown in Tab. 3, where the Sequential method yields the best performance.

Table 3. Comparison experiments of different interaction order in the proposed complementary serialization.

Method	mAP $\uparrow$	NDS $\uparrow$
Parallel	68.0	72.2
Sequential	<b>68.5</b>	<b>72.6</b>

### C. Visualization Results

To evaluate the qualitative results of UniMamba, we conduct a visual comparison of detection results with the previous state-of-the-art method, SAFDNet [49]. As shown in Fig. 1, UniMamba demonstrates superior performance. For instance, pedestrians that are not detected by SAFDNet in the first column are successfully detected by UniMamba, and UniMamba’s localization performance for vehicles also outperform those of SAFDNet. These results confirm that the flexible receptive field of UniMamba is effective in enhancing the model’s detection capabilities.